A HIGH RESOLUTION SPELEOTHEM RECORD FROM NE INDIA: PALEOSEISMIC AND MODERN CLIMATE INSIGHTS THROUGH U-TH AND $\delta^{18}O$ ANALYSIS

By

Christopher G. Myers

Thesis

Submitted to the Faculty of the

Graduate School of Vanderbilt University

in partial fulfillment of the requirements

for the degree of

MASTER OF SCIENCE

in

Earth and Environmental Sciences

August, 2014

Nashville, Tennessee

Approved:

Jessica L. Oster, Ph.D.

Steven L. Goodbred, Jr., Ph.D.

ACKNOWLEDGMENTS

First and foremost, I would like to thank my advisor, Jessica Oster. I couldn't have done any of this work without Jessica's guidance and support. I have become a stronger scientist under her direction. I'm very grateful for all she has taught me, and the amazing opportunities she has presented me with. I would like to thank my thesis committee members, Steve Goodbred and Larissa DeSantis for their thoughtful guidance over the past two years. I would like to especially thank Steve Goodbred for his insight and support throughout my research endeavors.

I would like to thank my collaborators Sebastian Breitenbach and Warren Sharp for their professional guidance and support both in the field and in the laboratory. I would like to acknowledge Gregory Diengdoh for his relentless support in the field, and Christina Polito for her assistance in the lab.

I would like that thank my funding agencies at Vanderbilt University, the Cave Research Foundation, the Geological Society of America and the BanglaPIRE group. Their financial support was crucial to completing my fieldwork in NE India, and funding my analytical efforts.

I would like to thank all of the graduate students, faculty and staff of the Vanderbilt EES department. You are great people, and you have significantly shaped my life over the last two years. A special acknowledgment is directed toward David Furbish, Jonathon Gilligan, and Aaron Covey for their encouragement and assistance in my thesis research.

I owe immense gratitude to my friends and family who have supported my aspirations and kept me going. Lastly, but most importantly, I would like to acknowledge my wife, Megan. I have no idea how I would have done this without her, and I appreciate all she has done over the last two years to support, motivate, and encourage me each and every day.

TABLE OF CONTENTS

LIST OF TABLES

LIST OF FIGURES

CHAPTER I

Thesis Introduction

The state of Meghalaya in NE India is a vibrant landscape where the people are intimately tied to the regional geology and seasonal climate. The east-west oriented Shillong Massif dominates the topography of Meghalaya with steep cliffs and gorges to the south and rolling hills to the north. During the summer months, the Indian Summer Monsoon (ISM) brings immense rainfall, making Meghalaya the rainiest place on earth. In contrast, the winter months in Meghalaya are dry and often accompanied by water shortages (Breitenbach et al., 2010). The people of Meghalaya rely heavily upon the rainfall associated with the ISM, and any reduction in summer precipitation can drastically affect crop yields (Douglas et al., 2009). The ISM has been identified as a large-scale global climate "tipping element" with the possibility of rapid destabilization and reduction in rainfall in the event of increased planetary albedo due to aerosol forcing and/or land-use change (Lenton et al., 2008). Predicted changes in ocean-atmosphere climate systems due to anthropogenic warming, such as increased El Niño amplitude (Guilyardi, 2006), also have the ability to restrict ISM strength (Kumar et al., 2006). As the global climate continues to warm and the Indian population continues to grow, there is a strong need to understand how the ISM will behave in a warming future climate.

The intensity of the ISM in Meghalaya is a direct consequence of the steep orography and regional elevation, which in turn resultd from active tectonic uplift and deformation. Such tectonic activity results from Meghalaya's position at the junction of the Himalayan frontal arc to the north and the Burma arc to the east. The east-west trending Dauki Fault

separates Meghalaya from Bangladesh to the south. Tectonic convergence along the Dauki Fault is responsible for the uplift of the Shillong Massif (Chen and Molnar, 1990; Khattri, 1992) and has resulted in major seismic events such as the 1897 Great Assam Earthquake with an estimated 8.2 magnitude (Morino et al., 2011). The last major earthquake to affect Meghalaya was the 8.7 magnitude Assam-Tibet earthquake of 1950. Meghalaya's position in this tectonically active region along with the third fastest growing population in India (MeghalayaPopulation, 2013) renders its human population at risk of future mega earthquake events (Saikia, 1981). The current seismic history of NE India is only constrained to the last 1,500 years and as the regional population continues to grow, a better understanding of future seismic hazard is necessary (Sukhija et al., 1999; Bilham, 2013).

Along with producing large seismic events, uplift of the Shillong Massif in Meghalaya has exposed massive limestone deposits along the steep, south-dipping limb of the massif. These extensive limestone deposits have allowed for intense karstification of the southern margin of the massif, producing over 1,300 registered caves (Arbenz, 2012). Along with their intrinsic beauty, caves provide researchers with a unique way to study the physical processes that have acted upon the region. Secondary cave minerals, otherwise referred to as speleothems, present researchers with an important archive for studying various physical processes such as climate induced precipitation variations (Wang et al., 2008), fluctuations in vegetation history (Dorale et al., 1998), cave inhabitance by ancient hominids (Bischoff et al., 2007), and records of paleoseismic activity (Becker et al., 2006).

I.1 Overview of Thesis Research

Uranium-thorium (U-Th) dating methods can provide precise radiometric dates on speleothem carbonate material (Richards and Dorale, 2003). The use of speleothems as

paleoseismic archives have been applied in numerous regions (Kagan et al., 2005; Forti, 2001; Gilli, 2005; Becker et al., 2006; Panno et al., 2009), but this method has yet to be applied in NE India. Given the proximity of caves on the Shillong Massif to faults that are associated with large historic earthquakes, dating broken speleothems in NE India could expose a currently unexploited archive for paleoseismic events in this region (Kagan et al., 2005). Current research focuses on validating this method by dating speleothems broken during observed mega earthquake events to allow for a stronger understanding of how broken speleothem may used as paleoseismic archives of events prior to the observed historic record. A stronger understanding of the seismic history of NE India would aid in the evaluation of a possible reoccurrence interval for mega earthquakes in this region.

Part I of this thesis describes the outcome of evaluating the use of speleothems in NE India as recorders of past seismic events along the faults bounding the Shillong Massif. As part of the current study, fractured stalagmites and collapsed soda straws were collected and dated using U-Th methods to reveal the ages of breakage events. Results from this study reveal that speleothems in caves along the southern margin of the Shillong Massif likely fracture during seismic events and have the potential to extend the seismic record in this region beyond limited historical accounts. Continued research using speleothems as paleoseismic archives in NE India will illuminate seismic risks and should hopefully provide motivation for enforcing stricter building code regulations and safety protocols in this populous region.

Oxygen isotope ratios (δ^{18}O) in speleothem carbonate are commonly analyzed as a proxy for the isotopic composition of rainfall over a given region and can reveal changes in precipitation moisture source, transport pathway, temperature, and precipitation amount (Lachniet, 2009). Understanding the connection between speleothem proxy records and regional meteorology is crucial when interpreting speleothem δ^{18}O as a paleoclimate record.

Although δ^{18}O records from NE Indian speleothems have been interpreted as recording variations in ISM strength over centennial and millennial timescales (Sinha et al., 2011), seasonal variations in rainfall δ^{18}O measured over two years in Meghalaya were found to be most strongly influenced by variation in precipitation source and transport pathway rather than rainfall amount (Breitenbach et al., 2010). Proxy records from Meghalaya speleothems that grew recently and can be compared to the meteorologic record could provide calibration datasets that help to clarify the relationship between oxygen isotopes in regional precipitation, ISM strength, and global climate change.

Part II of this thesis presents a high resolution oxygen isotope time series from a speleothem from Mawmluh Cave that is aimed at calibrating the relationship between speleothem δ^{18}O and regional climate over the past several decades. This record of seasonal δ^{18}O variations in an annually laminated aragonite stalagmite covers 1957 to 2011 and can be compared with the instrumental record of meteorological variability in the region. This record reveals the same seasonal signal observed in NE India rainwater δ^{18}O and Mawmluh Cave drip water δ^{18}O (Breitenbach et al., 2010, 2014). This seasonally resolved record facilitates comparison between speleothem δ^{18}O and global indices of climate variability such as the Niño3 SST index as a proxy for El Niño Southern Oscillation (ENSO) variability. As such, this research may provide a useful calibration tool to aid in the interpretation of long-term speleothem records from this region and their relationship to ISM strength and variability previous to the observed meteorological record. A stronger understanding of ISM variability during the past will assist in the prediction of ISM variability for future monsoon seasons.

CHAPTER II

Paleoseismology of the Shillong Massif, India: Constraints from U-Th dating of tectonically broken cave deposits

II.1 Introduction

The state of Meghalaya in northeast India has the third fastest growing population in the country. Over the last decade the population has increased by almost 30% (MeghalayaPopulation, 2013). To the south, Bangladesh, a country no bigger that the state of Iowa, has a population of over 160 million people making it the most densely populated country in the world (BanglaPIRE, 2013). The Shillong Massif, within the state of Meghalaya just north of the Bangladesh-India border, is positioned at the convergence zone of three tectonic plates and juncture of the Himalaya and Burma Arcs (Figure II.1). The Shillong Massif is separated from northeast Bangladesh by the east-west trending Dauki fault (Figure II.1). This north dipping thrust fault along the southern margin of the Shillong Massif is believed to have been active throughout the Quaternary based on uplifted late Tertiary and Quaternary sediments found along the southern boundary of the Massif (Morino et al., 2011). Furthermore, tectonic activity along the Dauki fault system is believed to be linked with several historically documented seismic events including the estimated magnitude 8.2 Great Assam earthquake of 1897 (Morino et al., 2011).

Due to rapid population growth in this region, the prevalence of poverty, and lack of building code and regulations, the people and infrastructure of Bangladesh and northeast India are not well prepared for mega-earthquake events (Bilham, 2013). The historic record

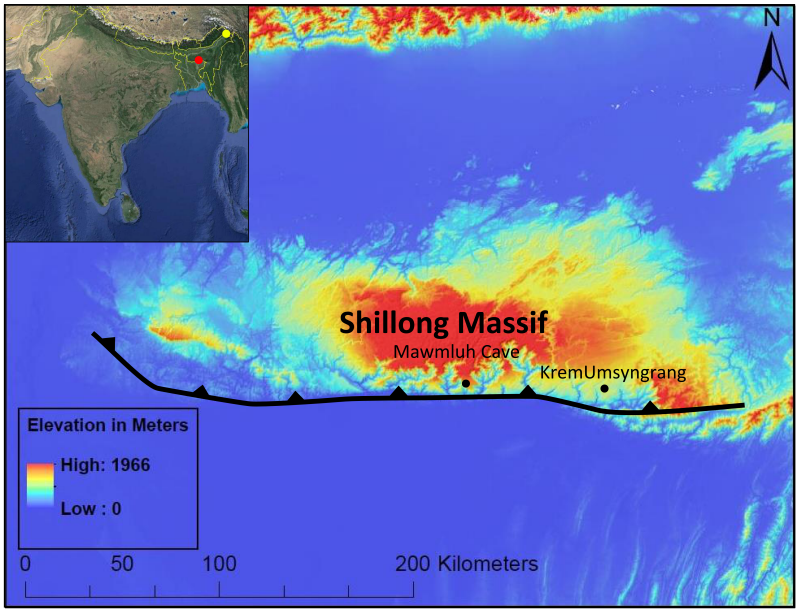

Figure II.1: Regional Map of NE India. Mawmluh Cave and Krem Umsyngrang are both located on the southern margin of the Shillong Massif as symbolized by black dots. The Dauki Fault (thick black line) is located along the southern limb of the Shillong Massif. Map insert shows the location of the Shillong Massif (red dot) directly above the NE border of Bangladesh and the epicenter of the estimated 8.7 magnitude Assam-Tibet earthquake of 1950 (yellow dot)

of seismic events in northern Bangladesh and northeast India extends back to approximately 1500 AD (Sukhija et al., 1999), with major earthquakes in 1548 AD, 1664 AD, and the Great Assam earthquake of 1897 considered to be associated with seismic activity along the Dauki fault system (Morino et al., 2011). Primary surface ruptures have been observed along the Himalayan front, yet the lack of observable ruptures around the Shillong Massif limits adequate reconstruction of past seismic events in this area (Reddy et al., 2009). Previous paleoseismic studies of the Meghalaya region have relied upon secondary sedimentary features such as liquefaction, deformation, and slump zones observed in surface ruptures as the primary proxies for previous earthquake events (Reddy et al., 2009). Radiocarbon dating of uprooted plant material found in liquefaction induced sedimentary features has been used to constrain the ages of paleoseismic events along the Shillong Massif (Sukhija et al., 1999). Paleoseismic ages from these studies suggest a recurrence interval of 400-600 years for mega-earthquakes on the massif (Sukhija et al., 1999). However, the lack of observable

surface ruptures, the inability to date events beyond ∼50,000 years bp, and large errors (± 150 years) associated with radiocarbon dating limit the accuracy and temporal span of this approach (Sukhija et al., 1999).

The dating of broken speleothems, or secondary cave deposits, provides an alternative approach to paleoseismology in regions such as Meghalaya where surface ruptures suitable for dating are limited and caves are present. Speleothems are comprised of carbonate material such as calcite, aragonite, or gypsum that form within a cave system upon chemical precipitation of infiltrating drip water. Speleothem carbonate material can be reliably dated using high-precision uranium-series techniques (Richards and Dorale, 2003). Uranium, which tends to be soluble in oxic environments, is co-precipitated with speleothem carbonate material and the in-growth of Th can be measured to date speleothem carbonate material that precipitated over the last 500,000 years (Richards and Dorale, 2003). Broken speleothems have been used successfully as archives of seismic event ages in several regions, including the Dead Sea (Kagan et al., 2005), Italy (Forti, 2001), Slovenia (Gilli, 2005), France (Gilli, 2005), Germany (Becker et al., 2006), and the New Madrid Fault Zone in the Midwestern United States (Panno et al., 2009). Given the close proximity of Shillong Massif caves to active faults, seismic waves associated with mega-earthquakes such as the Great Assam of 1897 likely had the ability to fracture speleothems and produce paleoseismic archives that can be dated precisely. This hypothesis is tested here by constraining speleothem breakage event ages using uranium-thorium (U-Th) dating methods on speleothems collected from caves along the southern margin of the Shillong Massif.

II.2 Speleothem Paleoseismology

Speleothems undergo various types of damage during large earthquake events such as fracturing and collapse of stalagmites and fracturing of stalactites and soda straws (Kagan et al., 2005; Becker et al., 2006). Broken speleothems are not only paleoseismic indicators of proximal tectonic movements, but may also record more distal tectonic events (Gilli, 1999). Figure II.2 depicts models of speleothem damage due to seismic events and possible examples of such features from caves in NE India. Figure II.2a depicts a sub-horizontally sheared stalagmite with secondary growth forming on the newly exposed surface. Previous research using broken speleothems as paleoseismic archives has indicated that breakages similar to that shown in Figure II.2a are indicative of being fractured through large earthquake events (Forti, 2001). Figure II.2b shows a stalagmite breakdown structure similar to Figure II.2a taken from Krem Umsynrang, a cave on the southern margin of the Shillong Massif. The bottom of the secondary growth in Figure II.2b can be dated, as well as the top of the fractured old growth portion to constrain the age of the causal event. Thin soda straw stalactites as seen in Figure II.2c are often broken in earthquake events (Panno et al., 2009). The growing end of broken soda straws can be dated to obtain the most recent age of soda straw growth before breakage. Figure II.2d is another photo from Krem Umsynrang where multiple generations of broken soda straws are found around the base of a collapsed stalagmite with multiple locations of new growth on the collapsed feature.

It should be noted that breakdown of speleothems is not exclusively caused by seismic events. Other natural processes such as flooding, ice intrusion, and failure of unconsolidated sediments in the cave may also break speleothems (Becker et al., 2006). Furthermore, human use of caves both historically and for tourism may induce speleothem breakages that should not be misinterpreted as being produced by seismic events.

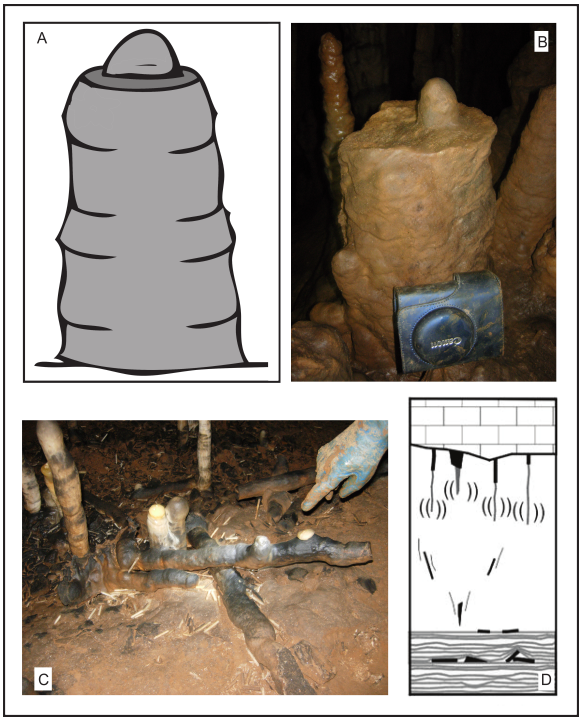

Figure II.2: Examples of broken stalagmite structures used in paleoseismology. (A) and (C) after Kagan, 2005 and Becker, 2006 respectively. (B) and (C) photo credit: Sebastian Breitenbach.

II.3 Study Location

Two caves in NE India, Mawmluh Cave and Krem Umsyngrang, were investigated for speleothem paleoseismic research. Both caves are positioned on the southern margin of the Shillong Massif, directly north of the east-west trending Dauki fault (Figure II.1). Although the central and northern parts of the massif are devoid of karst, the Shella Limestone and Therria Sandstone formations dominate the southern margin of the Shillong Massif and have been heavily karstified through Indian summer monsoon (ISM) rainfall (Gogoi et al., 2009). Over 1,300 caves have been registered along the southern fringe of the Shillong Massif, making it the highest density region of caves in India (Arbenz, 2012).

Mawmluh Cave and Krem Umsynrang are both contained within the Shella Formation of the mid-upper Paleocene (Arbenz, 2012). Within the Shella formation, Mawmluh cave

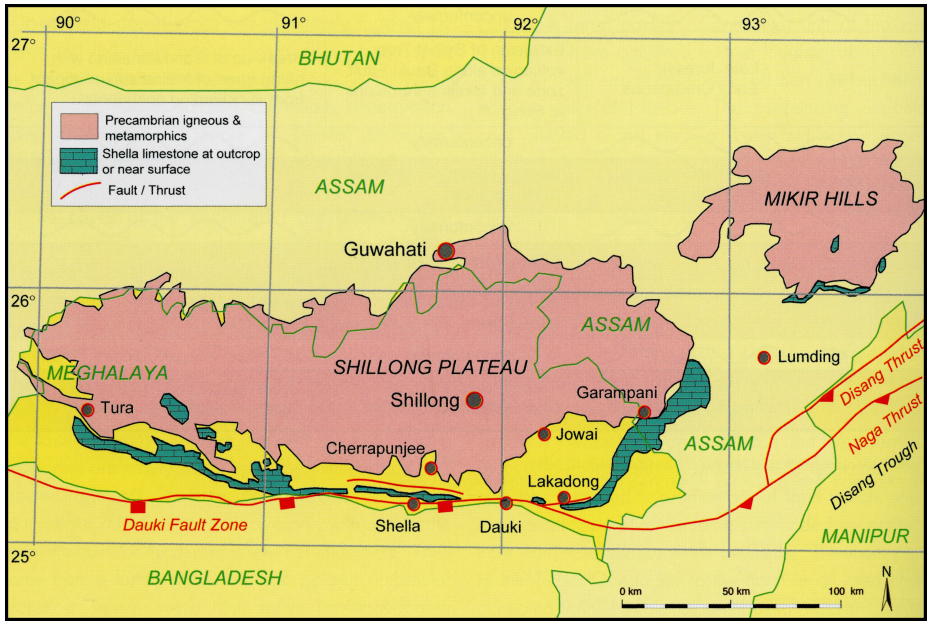

Figure II.3: Regional geological map of Meghalaya showing main structures, location of the Dauki Fault Zone, and the Shella Limestone Occurrence. Based in part on Geological Survey of India (1981, 2009) (Arbenz, 2012).

formed along the contact between the Lakadong Limestone and Therria sandstone units (Arbenz, 2012). Mawmluh Cave is a 7 km long sub-horizontal system that follows the path of the Mawmluh River that flows into the caves main entrance 1,160 m above sea level. Mawmluh Cave is overlain by 30-100 m of host rock consisting of limestone, sandstone, and a thin coal layer (Breitenbach et al., 2014). Krem Umsynrang is located in the Jaintia Hills region of NE India, approximately 25 km southeast of Jowai, Meghalaya. Krem Umsynrang is a sub-horizontal limestone cave approximately 5.6 km in length and is situated within the Lakadong Limestone unit of the Shella Formation.

II.4 Methods

II.4.1 Sample Collection

Broken speleothems and new carbonate growth were collected from Mawmluh Cave and Krem Umsyngrang in February of 2013 and March of 2014. Care was taken while caving to avoid collecting speleothems from areas where human traffic, loose cave sediments, or active cave streams clearly might have caused speleothem breakage. The entire broken speleothem was taken if possible, but in some situations a hammer and chisel were used to separate the new growth from the fractured surface. When a hammer and chisel were needed, the interface between the fractured surface and the base of the new growth was preserved to capture the inception of new growth after the breakage event. In an attempt to identify structures that may have broken during the well-documented 1950 and 1897 earthquakes, broken speleothems associated with small, actively growing post-breakage formations (2cm - 10cm) were preferentially sampled. Overall, six breakdown structures and 18 fractured soda straws were sampled between the two caves over both field seasons.

II.4.2 Sample Preparation

Sub-samples for U-Th dating were collected from the top of the old growth and the bottom of the new growth portions of each breakdown structure in an attempt to constrain the age of the causal breakage event. All stalagmites were slabbed longitudinally along the growth axis to identify the oldest and youngest layers. ImageJ photo processing software was used for greyscale layer-counting of the scanned stalagmite images. The layer-counts were used to confirm the visual interpretation of the youngest and oldest layers and reference which layers dating samples were taken from. Soda straws were also imaged to

determine if one of the ends appeared to have been actively growing at the time of breakage.

Some stalagmites contained calcite-aragonite transitions at the interface between new and old growth, which is recognized by a change in crystal structure from columnar palisade calcite to acicular aragonite crystals. Aragonite is prone to post-deposition alteration to calcite in speleothems that are exposed to under-saturated infiltrating water. During aragonite to calcite alteration, uranium ions can be mobilized and removed from the carbonate, making the speleothem unsuitable for U-Th dating (Frisia et al., 2002). Calcite-aragonite transitions in our samples were examined under plane and cross-polarized light in thin section to confirm all dating horizons were composed of primary carbonate material prior to powder collection for U-Th dating analysis. To determine the amount of dating material necessary for U-Th analysis, samples for initial U concentrations were collected from the speleothems surface with a hand drill.

Powders for U-Th dating were collected from the slabbed stalagmites using a CM-2 micromilling system at Vanderbilt University. The micromill allows for precise sample collection along a single growth lamination. Powders were collected from 1 cm long trenches to a depth of 1000 μm. Powders were sampled from speleothem tops using a hand drill. A one-centimeter square was scoured to a depth of approximately 100 μm from the speleothem surface to remove any detrital contaminants before the powder was collected to a depth of approximately 500 μm. Powder samples for dating were also collected from the fallen soda straws using the hand drill. The growth ends of the soda straws were first gently abraded with the hand drill to remove detrital material prior to powder collection.

Sample Name	Sample Type	Wt (mg)	U (ppm)	^{232}Th (ppm)	^{230}Th/^{232}Th	^{232}Th/^{238}U	%err	^{230}Th/^{238}U	%err	^{234}U/^{238}U	%err	Detr-Uncorr Age (ka)	Detr-Uncorr Err (2s)	Detr-Corr Age (ka)	Detr-Corr Err (2s)	Initial ^{234}U/^{238}U		Date (C.E.)	Err (2s)
MAW 01-01	SS	26.41	47.47	0.0026	3.99	1.71E-05	1.04	6.48E-05	4.70	0.886	0.42	0.0080	0.0004	0.0062	0.0010	0.886	±0.004	**2007.3**	1.0
MAW 01-02	SS	27.65	60.91	0.0074	2.30	3.94E-05	0.85	8.69E-05	7.84	0.897	1.00	0.0106	0.0008	0.0066	0.0022	0.897	±0.009	**2007.0**	2.2
MAW 01-03	SS	17.76	72.18	0.0251	2.60	1.13E-04	0.95	2.91E-04	5.48	0.865	0.68	0.0367	0.0020	0.0249	0.0064	0.865	±0.006	**1988.7**	6.4
MAW 02-01 High	Stal	14.04	43.44	0.0027	2.71	1.81E-05	0.62	3.98E-05	12.6	0.930	0.60	0.0047	0.0006	0.0024	0.0011	0.930	±0.006	**2011.1**	1.1
MAW 02-01 Low	Stal	13.04	49.20	0.0024	25.9	1.41E-05	1.39	4.03E-04	4.81	0.892	1.20	0.0493	0.0024	0.0478	0.0025	0.892	±0.011	**1965.7**	2.5
MAW 03-01 Low	Stal	13.14	37.61	0.0030	19.6	2.41E-05	0.69	5.05E-04	2.66	0.899	0.58	0.0613	0.0017	0.0589	0.0021	0.899	±0.005	**1954.7**	2.1
MAW 04-01	SS	14.89	61.89	0.0117	2.93	6.10E-05	0.89	1.73E-04	2.93	0.916	2.00	0.0206	0.0007	0.0146	0.0031	0.916	±0.018	**1999.0**	3.1
MAW 04-02	SS	30.03	56.36	0.0016	11.4	8.40E-06	2.99	9.88E-05	4.72	0.928	2.40	0.0116	0.0006	0.0108	0.0007	0.928	±0.022	**2002.8**	0.7
MAW 04-03	SS	20.43	61.87	0.0020	10.0	9.78E-06	1.62	1.01E-04	2.38	0.916	1.80	0.0120	0.0004	0.0111	0.0006	0.916	±0.016	**2002.5**	0.6
MAW 04-05	SS	45.14	52.67	0.0108	2.26	6.72E-05	1.89	1.49E-04	5.71	0.905	0.94	0.0180	0.0010	0.0113	0.0036	0.905	±0.009	**2002.2**	3.6

Table II.1: All isotope ratios are activity ratios. Errors are 2-sigma. Detritus-uncorrected ages are calculated from measured ratios. Detritus-corrected ages were corrected for initial ^{230}Th assuming that measured ^{232}Th reflects detritus with (^{232}Th/^{238}U) = 1.21 $\pm$ 0.5 , (^{230}Th/^{238}U) = 1.0 $\pm$ 0.1, and (^{234}U/^{238}U) = 1.0 $\pm$ 0.1; i.e., detritus with the Th/U ratio of average crustal silicate, with ^{230}Th and ^{234}U approximately in secular equilibrium. Decay constants are those of (Jaffey et al., 1971) for 238U and (Cheng et al., 2013) for ^{230}Th and ^{234}U. The detritus-corrected age of MAW 02-01 High, a "zero-age sample", is corrected for 0.5 year, the approximate time between collection and analysis. (^{234}U/^{238}U) initial is back-calculated from the measured ratio and corrected ^{230}Th age. Calendar dates (Dates C.E., common era) are calculated by subtracting detritus-corrected ages from the date of analysis (2013.56). Soda straws and new growth portions of collapsed stalagmites are denoted by sample type "SS" and "Stal" respectively.

II.4.3 U-Th Dating

Initial paleoseismic dating efforts have focused on samples from Mawmluh Cave due to their high initial U concentration (37.6-72.2 ppm) and low detrital ^{232}Th values (0.00157-0.0251 ppm), making them highly favorable for precise dating of young samples (Table II.1). U-Th sample preparation and analysis were performed at the Berkeley Geochronology Center using a Thermo Neptune Plus Multi-Collector-Inductively-Coupled-Mass-Spectrometer (MC-ICP-MS). Sample powders were dissolved in 7N HNO_3 and equilibrated with a mixed spike containing ^{229}Th, ^{233}U, and ^{236}U. The spike was calibrated using solutions of NBL CRM 145 and solutions prepared from a 69 Ma U ore from Schwartzwalder Mine, Colorado, USA (hereafter, SM) that has been demonstrated to yield concordant U-Pb ages (Ludwig et al., 1985) and sample-to-sample agreement of ^{234}U/^{238}U and ^{230}Th/^{238}U ratios. U and Th were separated using two stages of HNO_3-HCl cation exchange chemistry followed by reaction with HNO_3 and $HClO_4$ to remove any residual organic material. U and Th fractions were analyzed separately to reduce tailing effects on ^{230}Th. Measured peak heights were corrected for peak tailing, multiplier dark noise/Faraday baselines, instrumental backgrounds, ion counter yields, mass fractionation, interfering spike isotopes, and procedural blanks. Mass fractionation was determined using the gravimetrically determined ^{233}U/^{236}U ratio of the spike. The external reproducibility of ^{234}U/^{238}U and ^{230}Th/^{238}U ratios of SM solutions measured during each run was better than 0.2%. Activity ratios and ages were calculated using the half-lives of (Jaffey et al., 1971) for ^{238}U, (Holden, 1989) for ^{232}Th, and (Cheng et al., 2013) for ^{230}Th and ^{234}U. Correction for U and Th from detritus was made assuming detritus with activity ratios of (^{232}Th/^{238}U) = 1.2 $\pm$ 0.6, (^{230}Th/^{238}U) = 1.0 $\pm$ 0.1, and (^{234}U/^{238}U) = 1.0 $\pm$ 0.1, which correspond to average silicate crust in secular equilibrium. Ages and uncertainties were calculated with Isoplot 3.75 (Ludwig, 2010). Uncertainties of corrected ages include measurement errors and uncertainties associated with detritus corrections (Table II.1).

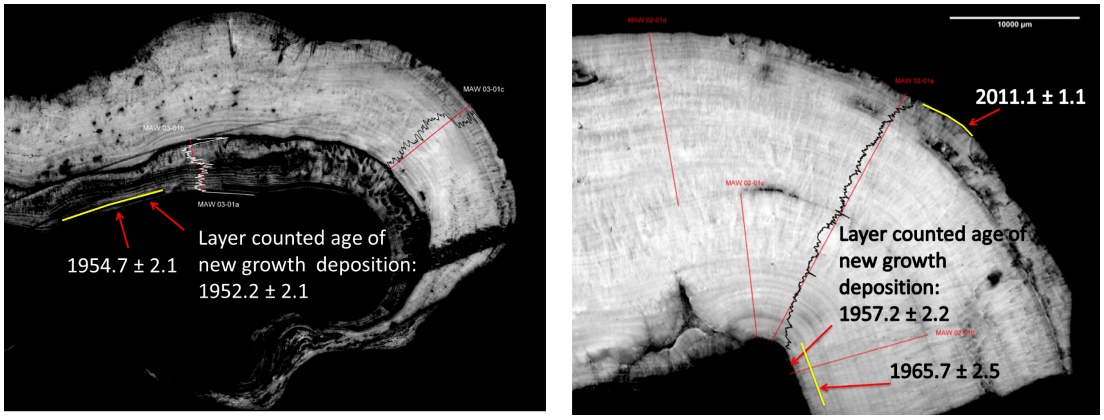

Figure II.4: Cross section greyscale images of MAW 02-01 on the left and MAW 03-01 on the right. All ages given are in Common Era (C.E.) and all errors are 2σ. Layer counting transect are shown along the stalagmite growth axis to quantify the number of annual layers present beneath the lowermost U-Th dating sample.

II.5 Results

To date, seven fallen soda straws, and two collapsed stalagmites from Mawmluh Cave have been analyzed for paleoseismic evidence. Broken soda straws collected from Mawmluh Cave reveal breakage dates ranging between 1988.7 and 2007.3 (C.E.). Analytical errors associated with the broken soda straws range between 6.4 and 0.6 years (all errors reported are 2σ) (Table II.1). The new-growth portions of the two collapsed stalagmite features, MAW 02-01 and MAW 03-01, have been analyzed for evidence of growth initiating after a seismic event. The MC-ICP-MS was specifically tuned to achieve precise results from young aragonite samples with high U concentrations. Dating priority was given to the new-growth portions of the two collapsed stalagmite structures because they are comprised of aragonite, and both of the old growth portions are comprised of calcite. The lower-most layers from the two new growth features, MAW 02-01 and MAW 03-01, have been dated to reveal ages of 1965.7 $\pm$ 2.5 years and 1954.7 $\pm$ 2.1 years respectively. The top of MAW 02-01, which was collected in February 2013, was dated as a zero-age sample and produced an age of 2011.1 $\pm$ 1.1 years.

Age clustering among the broken soda straws suggest three separate breakage events occurred in Mawmluh Cave. The soda straws that share similar breakage ages were found lying next to each other upon collection in 2013, indicating that they likely recorded the same causal breakage event. Although current data is limited to seven straws, results suggest that three separate breakage events in Mawmluh Cave occurred during the late 1980s, early 2000, and 2007 (Table II.1). Each of these hypothesized breakage events were recorded by multiple soda straws except the late 1980s event that was only recorded by MAW 01-03 (Table II.1).

Dating of the lower-most layers of the post-breakage growth on the two collapsed stalagmite structures from Mawmluh Cave produce U-Th ages of 1954.7 $\pm$ 2.1 (MAW 03-01) and 1965.7 $\pm$ 2.5 years (MAW 02-01) (Figure II.4). Layer counting results were used to quantify annual lamina present between the lowermost dating sample and the new growth-old growth transition. U-Th dating results along with the layer counting analysis has estimated the depositional age of MAW 03-01 and MAW 02-01 and to be 1952.2 $\pm$ 2.1 and 1957.2 $\pm$ 2.2 respectively (Figure II.4). Previous research in Mawmluh Cave performed by Sebastian Breitenbach (pers. comm.) has dated a separate small aragonitic stalagmite (MAW-4) deposited on a flowstone for a modern climate assessment. MAW-4 exhibits growth morphology similar to MAW 02-01 and MAW 03-01 and has a depositional age of 1954.0 $\pm$ 2.0 years (Cetti, 2012).

II.6 Discussion

Despite the clustering of soda straw breakage around the late 1980s, early 2000, and 2007, NE India experienced no mega earthquakes during these intervals. Lower-magnitude earthquakes are very common along the southern margin of the Shillong Massif and could

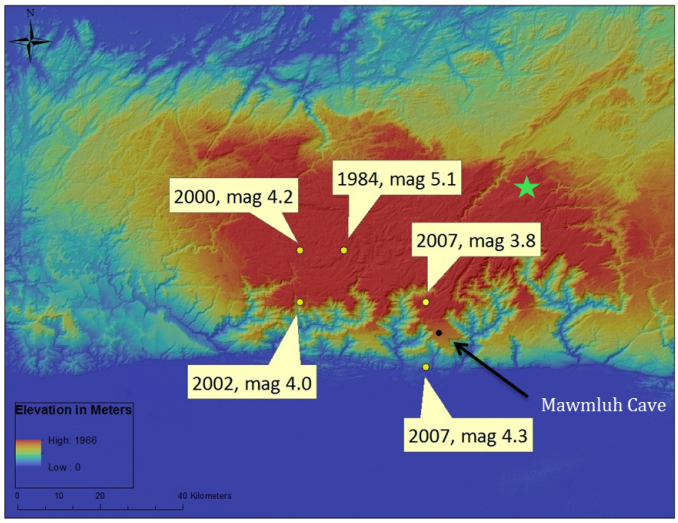

Figure II.5: Topographic map of the Shillong Massif. Location of Mawmluh Cave is shown with the black dot located southwest of Shillong as symbolized with the green star. Yellow dots represent the epicenters for the hypothesized seismic events recorded in the Mawmluh Cave soda straws. Seismic events were chosen on the criteria that they were the largest earthquakes with epicenters under 25km from Mawmluh Cave and occurred within analytical error of the clustered soda straw breakage events (Table II.1)

have caused the observed soda straw breakages. The earthquakes associated with the three soda straw breakage events are low in magnitude (3.8 to 5.1), however the epicenters of these events occoured within a 25 km radius of Mawmluh Cave (Figure II.5). It is also possible that soda straws from Mawmluh Cave were broken through human interference, unconsolidated sediment movement in the cave, or seasonal flooding of cave streams that were inactive upon collection. However, that latter two mechanisms likely would have either buried or displaced the soda straws following breakage, and human interference is likely to have crushed or shattered the straws during breakage. These suppositions, coupled with the abundance of low magnitude seismic events that occur along the southern margin of the Shillong Massif, support seismic interference as the most plausible explanation for the observed clusters of soda-straw breakage (Figure II.5).

The three fractured stalagmite new growth structures that have been analyzed from Mawmluh Cave have post breakage event depositional ages between 1952.2 $\pm$ 2.1 and 1957.2 $\pm$ 2.2 years. The evidence that all three of the new growth structures from Mawmluh

Cave were deposited shortly after 1950 suggests that the fractured stalagmite features from Mawmluh Cave may have broken during the 1950 Assam-Tibet earthquake. The 1950 Assam-Tibet earthquake was an estimated 8.7 Richter scale magnitude event that brought widespread destruction to NE India. Although the epicenter of this seismic event was in Tibet, approximately 365 miles northeast of Mawmluh Cave, the Brahmaputra Valley in NE India was strongly affected. Considerable structural damage and building collapse was documented in Shillong just 45 km northeast of Mawmluh Cave (USGS, 2014), and there were over 1,500 casualties in the area (Chamlagain, 2009). Although the old growth portions of the MAW 02-01 and MAW 03-01 breakdown features have yet to be analyzed, there is strong evidence with the new growth depositional ages presented here that broken speleothems in Mawmluh Cave may record the 1950 Assam-Tibet earthquake.

II.7 Conclusion

Numerous mega earthquakes have affected Northeast India and Bangladesh over the past $\sim$500 years of recorded history (Sukhija et al., 1999), but the mechanisms and recurrence of such events are not well understood. Due to the rapidly increasing population of northeast India and Bangladesh, as well as the prevalence of poverty and poor construction techniques the people living in this area are at risk of future large seismic events. Results presented here suggest that Mawmluh Cave on the southern margin of the Shillong Massif holds potential for elucidating the paleoseismic record through continued speleothem paleoseismology research. With U concentrations as high as 70 ppm, Mawmluh Cave allows for very precise dating of young speleothems (with 2σ errors of $\pm$ 0.6 to 6.4 years on samples 0.5 to 50 years old) which is imperative for accurate dating of structures that were fractured during the 1897 or 1950 earthquake events (Table II.1). U-Th dates of broken soda straws collected for this study have displayed clustering of breakage event ages that

might be associated with small magnitude seismic events in the late 1980s, early 2000, and 2007. U-Th dates from larger collapsed stalagmite features have produced post-breakage event ages in the early 1950s and that may reflect the Assam-Tibet earthquake of 1950. This evidence indicates that speleothems from Mawmluh Cave are likely being fractured in concurrence with regional seismic events.

The young ages and lack of correlation with known mega-earthquakes indicates that soda straws may be too reactive and break during proximal low magnitude events. Thus, to focus on large magnitude earthquakes future work should target larger collapsed stalagmite features for paleoseismic information. Currently, two additional collapsed stalagmite features from Mawmluh Cave, and three from Krem Umsynrang are being prepared for U-Th dating analysis at the Berkeley Geochronology Center. In addition to post-breakage growth samples already analyzed, dates on the pre-breakage portions of collapsed stalagmite features will help constrain the ages of causal seismic events. The additional paleoseismic dates will also assist in increasing the spatial and temporal resolution of our dataset. Future work will involve dating more speleothems from Mawmluh Cave along with numerous other caves along the southern margin of the Shillong Massif to look for evidence of speleothem breakage during the 1950 or 1897 earthquakes. The ability to extend the seismic record would allow for a more accurate estimate of mega earthquake reoccurrence in NE India and Bangladesh. As the human population continues to rise in this region, so does the need for a stronger understanding of the seismic risk and precautions people should be taking in the event of future mega earthquake events.

CHAPTER III

A Wavelet Analysis of Speleothem δ^{18}O and ENSO Frequency

III.1 Introduction

As the human population and water resource demand in India continue to grow at an unprecedented rate, the strength of the Indian summer monsoon (ISM) has never held such importance as it does in today's changing climate. The Indian summer months are dominated by the ISM, which seasonally brings immense rainfall and flooding to the southern, central, and northeastern parts of India. Droughts in India as a result of weak ISM precipitation can have dire consequences on India's agricultural output (Niranjan Kumar et al., 2013; Douglas et al., 2009). In 2002, severe drought in India due to weak ISM precipitation produced widespread crop failure and lowered the countrys Gross Domestic Product by approximately 1% (Gadgil et al., 2002)). As India's economy and human population continue to grow, so does the importance of understanding how modern climate change is affecting ISM dynamics.

The El Niño/Southern Oscillation (ENSO) is the most signficant climatic agent affecting ISM strength on interannual timescales (Kumar et al., 1999). Severe droughts in India due to weak ISM precipitation are strongly correlated with positive anomalies in ENSO strength (El Niño years) as recorded in SST indices of the equatorial Pacific Ocean (Kumar et al., 1999, 2006; Ashok et al., 2001; Krishnamurthy and Goswami, 2000; Shukla et al., 2011). However, not all strong El Niño events coincide with severe drought in India, such as the El Niño of 1997 when a strong prediction of weak monsoon rainfall proved false

(Kumar et al., 2006). In 2002 and 2004, normal monsoon rains were predicted along with moderate SST anomalies in the eastern tropical Pacific, however severe droughts occurred in central India (Gadgil et al., 2002, 2005).

One distinction between the 1997 El Niño, which did not correspond with ISM collapse, and the relatively weaker 2002 and 2004 events that did, is the anomalous location of SST maximums in the central Pacific Ocean associated with the latter (Yu et al., 2012). In fact, analysis of historical records indicates that failure of the ISM is more closely linked to the occurrence of these central Pacific SST anomalies as opposed to those El Niño events with SST anomalies located over the eastern Pacific (Kumar et al., 2006). The central Pacific "CP-El Niño" events have been growing in strength and frequency since the 1990s (Lee and McPhaden, 2010), a trend that could be linked with observed variations in ISM strength and precipitation trends on the Indian subcontinent. Here we evaluate very-high-resolution speleothem oxygen isotope δ^{18}O records from Northeast India that demonstrate sensitivity to changes in ENSO behavior over the past 53 years, highlighting their potential use in understanding ENSO-ISM dynamics beyond the historical record.

Mawmluh Cave (25°15'44"N and 91°52'54"E) in the Indian state of Meghalaya is located on the southern edge of the Shillong Massif directly north of the Bangladesh border at an elevation of 1160 m above sea level (Figure III.1). Meghalaya receives essentially all of its moisture from rain events during the monsoon season (May to September) (Breitenbach et al., 2010). Oxygen isotopes in rain and cave drip waters from Mawmluh are sensitive to changes in the source and transport pathway of monsoon rains (Breitenbach et al., 2010, 2014). Thus, speleothem δ^{18}O records from Mawmluh Cave should be sensitive to the regional atmospheric circulation response to changing ENSO dynamics over the past several decades.

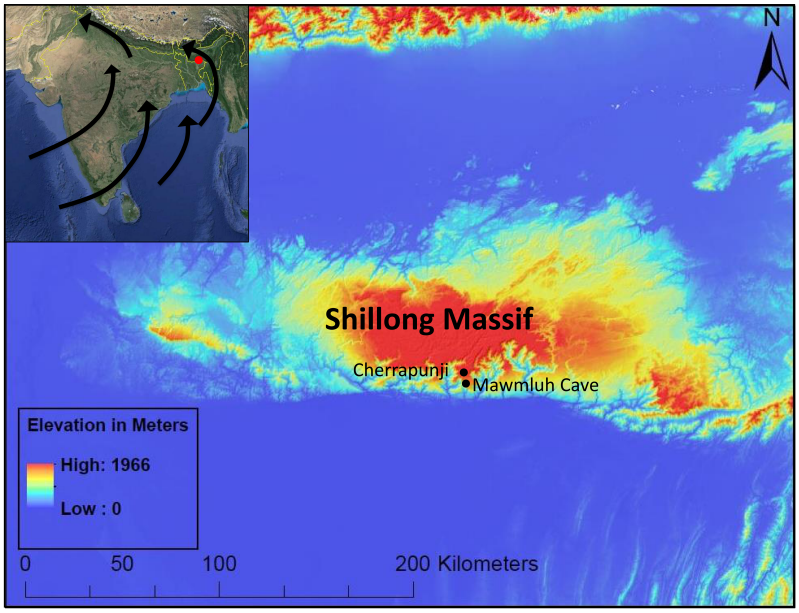

Figure III.1: Regional Map of NE India and Mawmluh Cave located on the southern margin of the Shillong Massif. Map insert shows the location of Mawmluh Cave (red dot) directly above the NE border of Bangladesh. Map insert also shows the seasonal direction of ISM precipitation events over the Indian subcontinent as illustrated by the black arrows

III.2 Methods

III.2.1 Sample Collection and Preparation

MAW 02-01 was an actively growing speleothem upon collection from Mawmluh Cave in February 2013. MAW 02-01 is composed of ∼2.2 cm of laminated aragonite that was deposited on the exposed surface of a fractured calcite stalagmite. A hammer and chisel were used to remove MAW 02-01 from the fractured stalagmite surface while preserving the calcite-aragonite interface. MAW 02-01 was precipitating from a soda straw fed drip 1.44 meters above the stalagmite surface. In March 2014 the averaged drip rate from the soda straw was observed to be approximately 41 seconds per drip.

MAW 02-01 was cut in half longitudinally along the growth axis to reveal growth laminae that are on average 3.8 mm thick. Each lamination consists of a light and dark couplet.

Petrographic analysis of a thin section from the base of 02-01 was used to characterize the carbonate material and look for evidence of diagenetic alteration. Five 1-pixel wide transects were drawn in ImageJ for greyscale layer-counting analysis on a scanned image of MAW 02-01. Each light colored peak in the layer counting analysis was coupled with an adjacent darker colored trough and counted as one annual year. Each transect was counted three times on three separate days to obtain an unbiased layer-count average.

III.2.2 Chronology

MAW 02-01 was mounted on a CM-2 micromill equipped with an Olympus SZX10 microscope and a NSK Volvere Max drill. Two $\sim$15 mg samples were drilled from MAW 02-01 for U-Th dating. Samples were taken adjacent to the layer counting transect at 0 and 20 mm depth from the top of the stalagmite. Before sampling the uppermost stalagmite surface, a square centimeter was gently abraded to a depth of 100 μm in order to remove any detrital material. The uppermost dating powder was collected with a hand drill from the pre-scoured square to a depth of .5 mm. Sample collection with the CM-2 micromill incorporated approximately two growth lamination per dating sample.

U-Th sample preparation and analysis were performed at the Berkeley Geochronology Center using a Thermo Neptune Plus Multi-Collector-Inductively-Coupled-Mass-Spectrometer (MC-ICP-MS). Sample powders were dissolved in 7N HNO_3 and equilibrated with a mixed spike containing ^{229}Th, ^{233}U, and ^{236}U. The spike was calibrated using solutions of NBL CRM 145 and solutions prepared from a 69 Ma U ore from Schwartzwalder Mine, Colorado, USA (hereafter, SM) that has been demonstrated to yield concordant U-Pb ages (Ludwig et al., 1985) and sample-to-sample agreement of ^{234}U/^{238}U and ^{230}Th/^{238}U ratios. U and Th were separated using two stages of HNO_3-HCl cation

exchange chemistry followed by reaction with HNO_3 and $HClO_4$ to remove any residual organic material. U and Th fractions were analyzed separately to reduce tailing effects on ^{230}Th. Measured peak heights were corrected for peak tailing, multiplier dark noise/Faraday baselines, instrumental backgrounds, ion counter yields, mass fractionation, interfering spike isotopes, and procedural blanks. Mass fractionation was determined using the gravimetrically determined ^{233}U/^{236}U ratio of the spike. The external reproducibility of ^{234}U/^{238}U and ^{230}Th/^{238}U ratios of SM solutions measured during each run was better than 0.2%. Activity ratios and ages were calculated using the half-lives of (Jaffey et al., 1971) for ^{238}U, (Holden, 1989) for ^{232}Th, and (Cheng et al., 2013) for ^{230}Th and ^{234}U. Correction for U and Th from detritus was made assuming detritus with activity ratios of (^{232}Th/^{238}U) = 1.2 $\pm$ 0.6, (^{230}Th/^{238}U) = 1.0 $\pm$ 0.1, and (^{234}U/^{238}U) = 1.0 $\pm$ 0.1, which correspond to average silicate crust in secular equilibrium. Ages and uncertainties were calculated with Isoplot 3.75 (Ludwig, 2010). Uncertainties of corrected ages include measurement errors and uncertainties associated with detritus corrections.

III.2.3 Stable Isotopes

Stable isotope powder collection was performed using the CM-2 micromill. Powders were collected at 50 μm spatial resolution along the layer-counted growth axis. In total 416 stable isotope powders were drilled along the 2.2 cm growth axis yielding seven to eight stable isotope samples per annual growth lamination.

Samples for stable isotope analysis were measured using a ThermoFinnigan GasBench II, equipped with a CTC autosampler, and coupled to a ConFlow IV interface and a Delta V Plus mass spectrometer following the methods described in (Breitenbach and Bernasconi, 2011). An in-house carbonate standard knows as MS2 was used to normalize the data

against the Vienne Pee Dee Belemnite (VPDB). Twenty-three of the 416 stable isotope samples were discarded during analysis on the ThermoFinnigan GasBench II due to inadequate sample size, resulting in 393 δ^{18}O samples.

III.2.4 Age-Depth Modeling

An age-depth model for MAW-02-01 was constructed using the MATLAB package, Constructing Proxy Records from Age models (COPRA) (Breitenbach et al., 2012). COPRA advances upon recently established techniques of anchoring precise time axis U-Th ages with layer counted chronologies to reduce the age model uncertainties in annually laminated speleothems (Domínguez-Villar et al., 2012). COPRA uses a least squares fit to estimate the minimum distance between the radiometric age model and the layer counted age model (Breitenbach et al., 2012). By incorporating the errors associated with the U-Th ages and the layer counting chronology, COPRA is able to transfer the age model uncertainties to the proxy record through Monte Carlo simulations. COPRA provides either the mean or median proxy value for every data point along with the associated error. Our COPRA age model was optimized with a linear interpolation of 2000 Monte Carlo simulations of the median isotope values with proxy confidence bounds and age model confidence bounds of 2σ.

III.2.5 Wavelet and Cross-Wavelet Analysis

Continuous wavelet transforms (CWT) were used to explore changes in the frequency of variability in the MAW 02-01 δ^{18}O record through time. In order to investigate linkages between the MAW 02-01 δ^{18}O record and the local climate, CWT analysis was performed on monthly rainfall anomalies recorded at the Cherrapunji meteorological station (coor-

dinates: 25°30'N, 91°70'E, 1313 m) and accessed online at http://climexp.knmi.nl/data-/t42515.dat. In addition, the following ENSO indicies were analyzed with CWT analysis to investigate possible linkages with the MAW 02-01 δ^{18}O record. The Oceanic Niño index (www.cpc.ncep.noaa.gov), Niño3 SST anomaly index (www.cpc.ncep.noaa.gov), and Niño4 SST anomaly index (www.cpc.ncep.noaa.gov) are indicies of sea-surface temperature (SST) anomalies in the equatorial pacific, specifically in the Niño-3.4, Niño-3 and Niño-4 regions respectively. The Southern Oscillation Index (www.cpc.ncep.noaa.gov/) measures sea level pressure differences between Tahihi and Darwin, Australia. The Western Hemispheric Warm pool (www.esrl.noaa.gov) measures a region of anomously warm SST off the western coast of Central America. The Pacific Decadal Oscillation (jisao.washington-.edu/pdo) is the leading empirical orthogonal function of monthly SST over the northern Pacific Ocean, and the Indian Ocean Dipole (www.jamstec.go) measures the east-west oscillation of SST anomalies in the Indian ocean. A cross-wavelet transform (XWT) and wavelet coherence transform (WCT) were performed with the individual CWT outputs to confirm the expected time-frequency relationships. A XWT analysis will expose areas in the two individual CWTs where a high common power is shared and define the phase relation shared over that interval. The WTC can be used to supplement the XWT by detecting locally phase locked behavior in the two CWTs that may not share high common power. All wavelet analyses were performed using a wavelet MATLAB package provided by the National Oceanography Centre of the Natural Environment Research Council (Grinsted et al., 2004).

Because CWT requires a constant sampling interval, our speleothem δ^{18}O time-series, which has varying time-steps ranging from .07 to .58 years, was interpolated to a monthly time-step in MATLAB. A linear, nearest neighbor, and shape preserving piecewise cubic Hermite interpolation (PCHIP) interpolation was performed on our speleothem δ^{18}O time-series and all yielded similar results. The simplest linear interpolation was chosen as our

age-model interpolation method for wavelet analysis.

All the indices used in our wavelet analysis were sufficiently close to a Gaussian distribution to not warrant further transformation of the data. The Morlet wavelet was used in all wavelet analyses. Indices were padded with the average dataset value on both sides of the series to bring the total length N up to the next highest power of two, thus increasing the Fourier transform time and reducing edge effects and uncertainties associated with the cone of influence (Grinsted et al., 2004).

III.3 Results

III.3.1 Chronology and δ^{18}O

Petrographic analysis of MAW 02-01 revealed clean and fibrous aragonite needles with no birefringence under cross-polarized light, which is indicative of primary aragonite material (Martín-García et al., 2009). U-Th analysis of MAW 02-01 has yielded an uppermost age of 2011.1(C.E.) $\pm$ of 1.1 years (2σ). The lowermost dating sample produced a U-Th age of 1965.7 (C.E.) $\pm$ 2.5 years (2σ). Layer-counting results of MAW 02-01 revealed 54 distinct layers between the top of the sample and the start of aragonite deposition, with a calculated standard error of 1.04 years averaged over the three recounts. MAW 02-01 δ^{18}O ranges from -3.33‰to -6.05‰(average -4.84‰) with an average external standard deviation of .056‰.

The COPRA age model assigns the bottommost δ^{18}O sample with an age of 1957.11 (C.E) $\pm$ 0.0031 years (2σ) and the uppermost sample an age of 2011.03 (C.E.) $\pm$ 0.0052 years (2σ). The average 2σ uncertainty on the age model is 0.005 years. The average 2σ

error associated with the median isotope values is 0.009‰. Based on U-Th chronology, MAW 02-01 grew at an average rate of 0.41 mm per year between 1957.11 and 2011.03.

III.3.2 Wavelets

Figure III.2 shows the continuous wavelet transformation (CWT) analyses above their associated time series for MAW 02-01 δ^{18}O, and the Niño3 SST anomaly index. Unlike the traditional Fourier analysis that is used to determine stationary frequency patterns in a time series, the wavelet analysis fits the time series into time-frequency space where localized and non-stationary frequencies can be observed (Grinsted et al., 2004).

A visual interpretation of the MAW 02-01 δ^{18}O time series reveals an increasingly negative trend in the average δ^{18}O signature from 1957 through 1962 (Figure III.2a). After 1962 the average δ^{18}O signature shows as increasingly positive trend through 1988, at which point the values become increasingly negative through 2011. A noticeable frequency change in the δ^{18}O time series can be observed beginning in 1975 and persisting through 1992. During this 17 year interval the δ^{18}O signature shows a significant annual periodicity, which is less pronounced prior to 1975 and after 1992. The MAW 02-01 CWT confirms these visual observations (Figure III.2a). Between 1975 and 1986 this annual frequency dominates the variability in the time series. The mid 1990s are defined by a strong four to six year frequency that is maintained through the end of the time series as well as a strong ten to twelve year frequency between 1995 and 2000. Prior to 1975 the four year frequency can also be observed, but not at the strength that is present in the mid 1990s.

Multiple ENSO indices that were evaluated using wavelet analysis (Niño3 SST Index , Niño4 SST Index, Oceanic Niño Index, Southern Oscillation Index, Pacific Decadal Os-

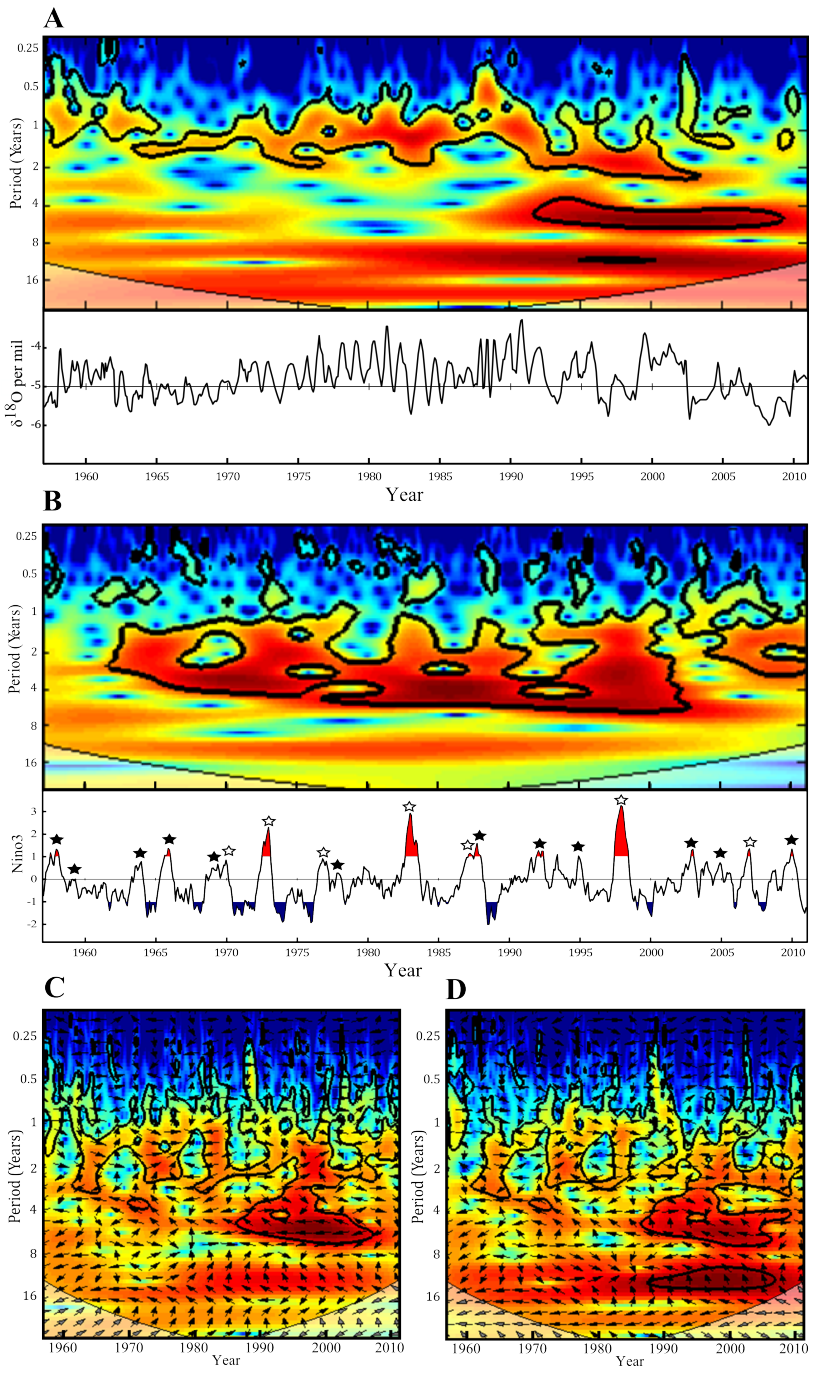

Figure III.2: Continuous wavelet transforms of MAW 02-01 δ^{18}O (A), and the Niño 3 SST anomaly index (B). CWTs are shown above their associated time series from 1957 through 2010. (B) Strong El Niño and La Niña years are shown in red and blue respectively and defined by a positive (El Niño) or negative (La Niña) SST departure from the mean of at least 1.0°C. Filled (empty) stars above the El Niño seasons denote the presence of a CP El Niño (EP El Niño) event as defined by (Yu et al., 2012). Cross-wavelet transforms are shown between MAW 02-01 δ^{18}O and Niño3 SST anomalies (C), and MAW 02-01 δ^{18}O and Niño4 SST anomalies (D). Color of the wavelet output define the time-frequency relationship with red depicting the strongest correlation, and blue the weakest. Areas within the black contour represent a shared frequency relationship above the 95% confidence interval. Arrow direction defines the phase relationship between the two indices for a given time and frequency. Right facing arrows represent an in-phase relationship, left facing represents anti-phase, and arrows pointing either up or down represent a lag or lead between the indices of 90° or 270°.

cillation, Western Hemispheric Warm Pool), showed similar period fluctuations. In this case Niño3 was chosen as our ENSO index for wavelet analysis due to its widespread use in ENSO related climate studies (Kawamura et al., 2005; Yeh et al., 2009; Kumar et al., 1999). Specifically, the Niño3 index tracks monthly resolved SST anomalies in the Niño 3 region of the eastern Pacific basin (5°North-5°South, 150°West-90°West), which differs from the Niño4 and Oceanic Niño Index that measure SST anomalies in the western and central Pacific Ocean. Throughout the Niño3 dataset the CWT shows significant periods between one and six years (Figure III.2b). Between 1965 and 2003 the Niño3 CWT displays a dominant four-year signal with a slowly increasing period. Between 2003 and the end of the time-series the Niño3 CWT frequency decreases to a dominant two year period.

The cross-wavelet transformation (XWT) between the MAW 02-01 and the Niño3 data sets (Figure III.2c) reveals a significant six-year period that is shared between both data sets from the late 1980s through 2010. The phase relationship during this interval is primarily anti-phase with a slight lag in MAW 02-01 behind Niño3 at the beginning of this interval, as signified by the slight variation in the phase angle arrows. The XWT between the MAW 02-01 and Niño4 data set (Figure III.2d) show the same frequency relationship seen in the Niño3 XWT in addition to a strong ten to twelve year frequency between the late 1980s and 2010.

III.4 Discussion

Historically, anomalies in Indian summer monsoon rainfall (ISMR) display a strong negative correlation with ENSO events (Krishna Kumar 1999, Ashok 2001, Krishnamurthy 2000, Shukla, 2011), with severe Indian droughts occurring during strong El Niño events (Krishna Kumar, 2006). The ENSO-ISM relationship fluctuates on interdecadal timescales,

varying between modes of stronger and weaker correlation (Ashok 2001, Kawamura, 2005). Understanding how speleothem archives in northeast India record these interdecadal fluctuations will allow for a better understanding of ISM variability prior to the instrumental record and assist in monsoon prediction and preparedness in the presence of a warming global climate.

III.4.1 MAW 02-01 δ^{18}O Signature

As long as cave air temperature remains somewhat constant, the δ^{18}O of speleothem carbonate should primarily record changes in the δ^{18}O of the drip water from which it grew, and this should reflect rainwater above the cave modified by evaporation and mixing of waters in the epikarst (Lachniet, 2009). Using (i) the aragonite-water fractionation equation of Kim et al. 2007, (ii) cave air temperature recorded at the site of speleothem collection in March and September of 2011 (18 to 22.5°C respectively), and (iii) the most recent (2010) MAW 02-01 δ^{18}O maximum and minimum (-5.97 to -4.61), we estimate δ^{18}O MAW 02-01 drip water values of -5.56 to -5.16‰. These values fall within the range of measured drip water δ^{18}O collected between 2011 and 2012 (-7.25 to -5.0‰)(Breitenbach et al., 2014). These results indicate that MAW 02-01 precipitated close to isotopic equilibrium with its drip water, and therefore the δ^{18}O variations documented from MAW 02-01 should primarily reflect changes in the δ^{18}O signature of rainwater and reflect changes in ISM moisture source and transport pathway.

The δ^{18}O values of 68 rainfall events sampled between March 2007 and October 2008 in Cherrapunji approximately 7.25 km southwest of Mawmluh Cave show no correlation with precipitation amount, nor do they indicate any influence of evaporative effects in the atmosphere. Rather, rainwater δ^{18}O in Meghalaya appears to vary primarily with the loca-

tion of source water and changes in moisture transport pathway (Breitenbach et al., 2010). The ISM moisture source source is known to vary seasonally from northwestern continental India into the open Indian Ocean and Arabian Sea at the onset of the ISM, and later into the Bay of Bengal during the late ISM season (Zhou and Yu, 2005; Breitenbach et al., 2010). The ISM influenced change in moisture source and transport pathway along with the freshening on the Bay of Bengal surface waters in the late summer and fall due to monsoon season runoff most strongly effect the annual changes in rainwater δ^{18}O in Cherrapunji (Breitenbach et al., 2010).

Drip water sampled from Mawmluh Cave in the same passage from which MAW 02-01 was collected reveals a strong seasonal pattern in δ^{18}O similar to that observed in NE India rainfall δ^{18}O (Breitenbach et al., 2014). This similar relationship suggests that the lag between a precipitation event on the surface and the water infiltrating into the cave system is quite short, on the order of a few weeks (Breitenbach et al., 2014). Thus, drip water, and therefore speleothem δ^{18}O in Mawmluh Cave should primarily reflect changes in precipitation moisture source and transport pathways, which are controlled by seasonal ISM variations. Additionally, we observe no correlation between MAW 02-01 δ^{18}O and the Cherrapunji Precipitation Index which measures anomalous monthly precipitation recorded in Cherrapunji between 1957 and 2010 (R2 = 0.00005), further indicating that MAW 02-01 δ^{18}O does not primarily reflect Cherrapunji rainfall amount, but rather is representative of seasonal changes in moisture source as observed in local rainwater δ^{18}O variations (Breitenbach et al., 2010).

III.4.2 Frequency Observations in MAW 02-01 δ^{18}O

The first major transition observed in the MAW 02-01 δ^{18}O CWT is the change from a dominant frequency of four to six years between 1957 and 1975 to a strong annual frequency that persists from 1976 to 1985 (Figure III.2a). A widely noted change in the frequency of ENSO variability occurred during the 1976-77 Pacific Ocean climate shift (Trenberth and Stepaniak, 2001; Krishnamurthy and Goswami, 2000; Kawamura et al., 2005; Kumar et al., 1999). The anomalously strong northern hemisphere winter of 1976-77 led to a deepened Aleutian low in the north Pacific region, which contributed to the transport of anomalously cool water into the central middle Pacific Ocean (Miller et al., 1994). The north Pacific ocean-atmosphere climate remained in this state for an additional ten years after 1976 and contributed to the decrease in ENSO frequency over this interval (Trenberth, 1990; Trenberth and Stepaniak, 2001). Analysis of ENSO SST indices and the ISMR index reveals that the negative correlation between ENSO and monsoon rainfall in central India weakened after 1976 (Kumar et al., 1999; Ashok et al., 2001). However, precipitation amounts in NE India are not always strongly correlated with the precipitation in central India, which is used to construct the ISMR (Parthasarathy et al., 1995), but are better represented by the meridional thermal gradient (MTG).

The MTG is a large-scale monsoon circulation index that represents the difference in area-averaged upper tropospheric (200-500 hPa) thickness between the Tibetan Plateau and the Indian Ocean (Kawamura et al., 2005). The MTG incorporates precipitation observed over the entire Indian subcontinent, and has been found to be a better indicator of precipitation in NE India (Kawamura et al., 2005)). The ISMR, MTG, and Niño3 index are all strongly correlated until 1975 (Kawamura et al., 2005), but after 1975, correlation of ISMR with both Niño3 and MTG weakens (Kawamura et al., 2005). Interestingly, the correlation between the MTG and Niño3 remains strong after 1975, indicating that the loss of ENSO-

ISM correlation at the 1976 Pacific Ocean climate shift may represent a shift in ISM spatial correlation from northwest-central India to northeast India (Kawamura et al., 2005).

This documented decrease in ENSO frequency between 1976 and 1986 due to the Pacific Ocean climate shift along with the hypothesized shift in ISM spatial correlation is evident in the MAW 02-01 δ^{18}O continuous wavelet transform (Figure III.2a). The absence of a strong four to six year frequency in the MAW 02-01 δ^{18}O CWT between 1976 and 1986 likely reflects the suppressed ENSO activity during this period. Prior to 1976 there is a one to two year seasonal signal present in the MAW 02-01 δ^{18}O CWT, however the power associated with the seasonal signal significantly increases during the 1976 to 1986 period. The shift to higher power associated with a seasonal signal in our δ^{18}O record between 1976 and 1986 likely reflects the loss of the four to six year ENSO frequency over this interval. As seen in the Niño3 time series, only the 1982-1983 El Niño occurred between 1975 and 1985, and there were no strong La Niña events during this interval (Figure III.2b). The suppressed ENSO frequency and lack of strong El Niño events, along with the shift in ISM spatial correlation over NE India between 1976 and 1986 likely accounts for the loss of the four to six year ENSO frequency and the prominence of the seasonal signal in our δ^{18}O record during this time.

III.4.3 A Modern change in El Niño Character

From 1985 until the end of the record in 2011, the four to six year ENSO frequency is at its strongest in the MAW 02-01 δ^{18}O CWT. The cross-wavelet transform between MAW 02-01 and the Niño3 index (Figure III.2c) indicates that the region of strongest ENSO frequency in the MAW 02-01 CWT (1990 to 2010) corresponds with a region of shared high common power with four to six year periodicity between MAW 02-01 and Niño3.

The phase relationship over the region of shared high common power is locked in an anti-phase state with the Niño3 index leading the MAW 02-01 time-series. We would expect the two time series to be phase locked over the interval of shared high common power if a cause and effect relationship is predicted (Grinsted et al., 2004). The phase locked relationship in the MAW 02-01-Niño3 cross-wavelet transform reaffirms that MAW 02-01 δ^{18}O variations are intimately related to ENSO frequency variations between 1990 and 2010. The high strength of the signal after 1985 might reflect the change in ISM spatial correlation over NE India, or it may be related to a different shift in El Niño behavior.

A change in the character of El Niño events in the equatorial Pacific has been observed since the early 1990s (Lee and McPhaden, 2010). Traditional El Niño events are distinguished by anonymously high SSTs in the eastern equatorial Pacific during northern hemisphere winters. Beginning in the early 1990s, El Niño events increasingly show maximum SSTs in the central equatorial Pacific with cooler water to the east and west (Ashok and Yamagata, 2009; Yeh et al., 2009). The atmospheric teleconnections associated with this central pacific El Niño (CP-El Niño) are different from those that act during eastern Pacific El Niño (EP-El Niño) events. Although CP-El Niño events have been occurring since 1953 (Yu et al., 2012), the frequency and strength of El Niño events occurring in the CP region have been increasing since the early 1990s (Figure III.2b) (Lee and McPhaden, 2010).

Historical records indicate that CP-El Niño is more strongly correlated with ISM droughts in central India than EP- El Niño (Kumar et al., 2006). This observation is supported by global circulation model experiments that suggest that CP-El Niño events are much more effective at forcing drought like conditions in India by shifting the descending arm of the Walker circulation over the Indian subcontinent. This westward shift of Walker cell circulation decreases ISM strength by weakening the thermal gradient between the Indian subcontinent landmass and the Indian Ocean (Kumar et al., 2006). CP-El Niño events are

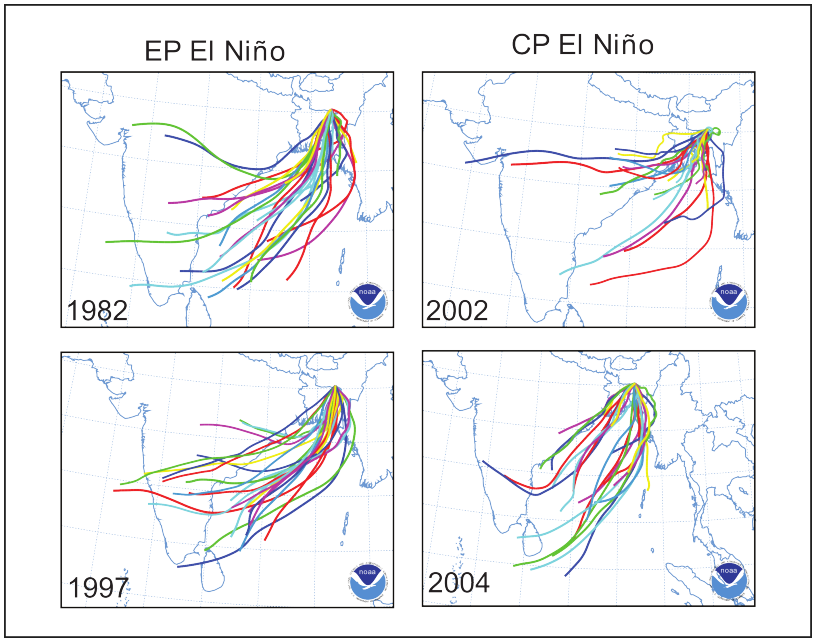

Figure III.3: Air mass back trajectories using NOAAs HYSPLIT model. Trajectories are computed 72 hours before the air mass reaches Mawmluh Cave for individual days between July 6th, and July 31st at a height of 1,500 meters above ground level. El Niño years were distinguished as EP or CP by Yu et al. 2012.

better represented by SST anomalies in the Niño4 region of the equatorial Pacific (160°E-150°W, 5°S- 5°N) than the Niño3 region, which is more representative of EP-El Niño events (Lee and McPhaden, 2010). MAW 02-01 δ^{18}O shows a stronger relationship with SST anomalies in the Niño4 versus the Niño3 region between the late 1980s and 2010 (Figure III.2c,d). This indicates that MAW 02-01 δ^{18}O is more directly related to frequency variations in CP-El Niño rather than EP-El Niño events.

The precipitation moisture source for NE India moves into the open Indian Ocean and Arabian Sea during peak ISM season (Breitenbach et al., 2010). However, the Walker circulation shift observed during a CP- El Niño is likely to modify this moisture source by suppressing oceanic moisture advection over the Indian Ocean. Hysplit back trajectory models suggest there is a distinct change in CP-El Niño moisture source trajectories during peak ISM season. Back trajectories for the month of July (peak monsoon season in Cherrapunji) during CP-El Niño years tend to originate more locally over the Bay of Bengal

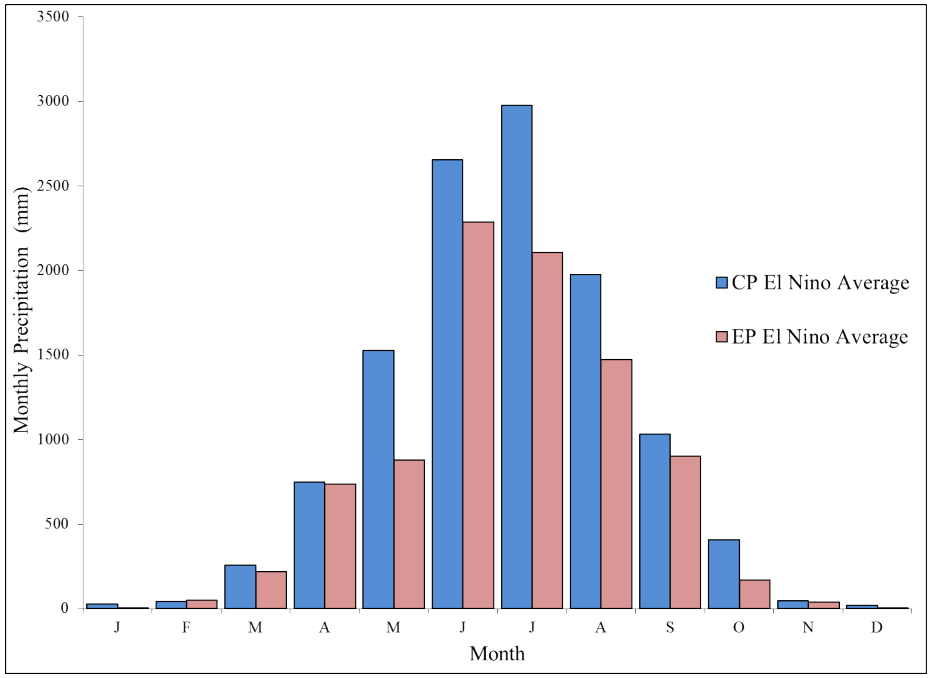

Figure III.4: Observed monthly precipitation in Cherrapunji India (http://climexp.knmi.nl/data/t42515.dat) averaged over all CP-El Niño or EP-El Niño years between 1957 and 2010 as defined by Yu et al., 2012. Annual precipitation averages of 8889 mm and 11732 mm for all EP-El Niños and CP-El Nios respectively between 1957 and 2010. Cherrapunji recives on average 32% more precipitation annually during CP-El Niños compared to EP-El Niños.

in comparison to the back trajectories for EP- El Niño events that tend to originate further west over the Indian peninsula (Figure III.3). This implies that during CP- El Niño years, a larger proportion of the moisture reaching NE India is sourced in the Bay of Bengal during peak ISM season, which is not observed until the late ISM season during EP- El Niño events (Breitenbach et al., 2010).

The Bay of Bengal experiences massive freshwater fluvial runoff from the Ganges-Brahmaputra river system during the ISM season (Breitenbach et al., 2010). An isotope mass balance box model estimates 20% to 50% of the δ^{18}O depletion observed in NE India precipitation is a result of the δ^{18}O depleted freshwater input into the Bay of Bengal through the Ganges-Brahmaputra river system (Breitenbach et al., 2010). Since 1957 Cherrapunji has received on average 32% more precipitation annually in years characterized by

CP- El Niño events compared to those characterized by EP-El Niño events (Figure III.4). The increased precipitation over NE India during a CP-El Niño should increase the fresh-water runoff into the Bay of Bengal, which should provide a more depleted δ^{18}O source for subsequent precipitation. The strong correlation between ISM strength and CP-El Niño events, along with the early shift in NE India moisture source into the Bay of Bengal and increased δ^{18}O depletion of Bay of Bengal surface waters likely controls the strong four to six year ENSO frequency and negative δ^{18}O trend between 1990 and 2010.

III.5 Conclusion

Wavelet analysis of δ^{18}O variations in an annually laminated speleothem from Mawmluh Cave in NE India documents ENSO influenced frequency variations between 1957 and 2010. Since ISM rainfall data became available in 1871, severe droughts in central India due to weak ISM rainfall are coincident with strong El Niño events (Kumar et al., 2006). However, NE India where MAW 02-01 was located has been shown to receive normal precipitation amounts while central India is experiencing drought like conditions, making NE India a good location to study ENSO induced changes in ISM moisture source and transport pathway (Gadgil et al., 2005). MAW 02-01 has recorded ISM fluctuations due to ENSO strength and frequency variations as seen in the loss of the four to six year frequency between 1975 and 1985 when ENSO variability was suppressed after the 1976 Pacific Ocean climate shift (Figure III.2a)

CP-El Niño events which have been increasing in strength and amplitude since the early 1990s have a stronger influence on ISM failure in central India as compared to traditional EP-El Niño events (Kumar et al., 2006). The increase in strength and amplitude of CP- El Niño events since 1990 is evident in the strong four to six year frequency between 1990 and

2010 in the MAW 02-01 δ^{18}O CWT (Figure III.2a). Increased precipitation over NE India during a CP-El Niño and depletion of δ^{18}O in the Bay of Bengal, along with an earlier ISM season moisture source shift into the Bay of Bengal during a CP event is likely the cause for the strong four to six year frequency and increasing negative trend in the MAW 02-01 δ^{18}O signature starting in 1990 (Figure III.2a).

The ability of NE Indian speleothems to record ENSO strength and frequency variations through rainwater δ^{18}O fluctuations has numerous implications for future speleothem paleoclimate work in NE India, as well as Indian monsoon preparedness. Although it is unclear how Pacific SST anomalies and El Niño behavior will be modified in a warming global climate, it is clear that CP-El Niño events have the ability to greatly affect precipitation over the Indian subcontinent. We have shown that speleothem δ^{18}O in Mawmluh Cave clearly records the change in El Niño character that began in the early 1990s. This connection between the terrestrial record and El Niño induced ISM fluctuations can be exploited in future NE Indian paleoclimate records to infer the ISM-ENSO relationship in the past. A stronger understanding of how CP-El Niño events have disrupted ISM precipitation over central India in the past will have pronounced societal impacts on ISM failure preparedness for CP-El Niño events in the future.

BIBLIOGRAPHY

Arbenz, T. (2012). *Cave Pearls of Meghalaya, Volume 1, Pala Range and Kopili Valley*. Abode of Clouds Project.

Ashok, K., Guan, Z., and Yamagata, T. (2001). Impact of the indian ocean dipole on the relationship between the indian monsoon rainfall and enso. *Geophysical Research Letters*, 28(23):4499–4502.

Ashok, K. and Yamagata, T. (2009). Climate change: The el niño with a difference. *Nature*, 461(7263):481–484.

BanglaPIRE (2013). BanglaPIRE life on a tectonically-active delta: Convergence of earth science and geohazard research in bangladesh with education and capacity building. http://www.banglapire.org/About. Accessed: 2013-12-03.

Becker, A., Davenport, C. A., Eichenberger, U., Gilli, E., Jeannin, P.-Y., and Lacave, C. (2006). Speleoseismology: a critical perspective. *Journal of seismology*, 10(3):371–388.

Bilham, R. (2013). Societal and observational problems in earthquake risk assessments and their delivery to those most at risk. *Tectonophysics*, 584:166–173.

Bischoff, J. L., Williams, R. W., Rosenbauer, R. J., Aramburu, A., Arsuaga, J. L., García, N., and Cuenca-Bescós, G. (2007). High-resolution u-series dates from the sima de los huesos hominids yields: implications for the evolution of the early neanderthal lineage. *Journal of Archaeological Science*, 34(5):763–770.

Breitenbach, S. F., Adkins, J. F., Meyer, H., Marwan, N., Kumar, K. K., and Haug, G. H. (2010). Strong influence of water vapor source dynamics on stable isotopes in precipitation observed in southern meghalaya, ne india. *Earth and Planetary Science Letters*, 292(1):212–220.

Breitenbach, S. F., Marwan, N., Meyer, H., Lechleitner, F., and Diengdoh, G. (2014). Influence of the indian summer monsoon on cave ventilation and drip water isotope signature. unpublished manuscript.

Breitenbach, S. F. M. and Bernasconi, S. M. (2011). Carbon and oxygen isotope analysis of small carbonate samples (20 to 100g) with a gasbench ii preparation device. *Rapid Communications in Mass Spectrometry*, 25(13):1910–1914.

Breitenbach, S. F. M., Rehfeld, K., Goswami, B., Baldini, J. U. L., Ridley, H. E., Kennett, D., Prufer, K., Aquino, V. V., Asmerom, Y., Polyak, V. J., Cheng, H., Kurths, J., and Marwan, N. (2012). Constructing proxy-record age models (copra). *Climate of the Past Discussions*, 8(3):2369–2408.

Chamlagain, D. (2009). Earthquake scenario and recent efforts toward earthquake risk reduction in nepal. *Journal of South Asia Disaster Studies*, 2(1):57–80.

Chen, W.-P. and Molnar, P. (1990). Source parameters of earthquakes and intraplate deformation beneath the shillong plateau and the northern indoburman ranges. *Journal of Geophysical Research: Solid Earth (1978–2012)*, 95(B8):12527–12552.

Cheng, H., Lawrence Edwards, R., Shen, C.-C., Polyak, V. J., Asmerom, Y., Woodhead, J., Hellstrom, J., Wang, Y., Kong, X., Spötl, C., et al. (2013). Improvements in¡ sup¿ 230¡/sup¿ th dating,¡ sup¿ 230¡/sup¿ th and¡ sup¿ 234¡/sup¿ u half-life values, and u–th isotopic measurements by multi-collector inductively coupled plasma mass spectrometry. *Earth and Planetary Science Letters*, 371:82–91.

Domínguez-Villar, D., Baker, A., Fairchild, I. J., and Edwards, R. L. (2012). A method to anchor floating chronologies in annually laminated speleothems with u–th dates. *Quaternary Geochronology*, 14:57–66.

Dorale, J. A., Edwards, R. L., Ito, E., and González, L. A. (1998). Climate and vegetation history of the midcontinent from 75 to 25 ka: a speleothem record from crevice cave, missouri, usa. *Science*, 282(5395):1871–1874.

Douglas, E., Beltrán-Przekurat, A., Niyogi, D., Pielke Sr, R., and Vörösmarty, C. (2009). The impact of agricultural intensification and irrigation on land–atmosphere interactions and indian monsoon precipitationa mesoscale modeling perspective. *Global and Planetary Change*, 67(1):117–128.

Forti, P. (2001). Seismotectonic and paleoseismic studies from speleothems: the state of the art. *Geologica belgica*, 4(3-4):175–185.

Frisia, S., Borsato, A., Fairchild, I. J., McDermott, F., and Selmo, E. M. (2002). Aragonite-calcite relationships in speleothems (grotte de clamouse, france): environment, fabrics, and carbonate geochemistry. *Journal of Sedimentary Research*, 72(5):687–699.

Gadgil, S., Rajeevan, M., and Nanjundiah, R. (2005). Monsoon prediction-why yet another failure? *Current Science*, 88(9):1389–1400.

Gadgil, S., Srinivasan, J., Nanjundiah, R. S., Kumar, K. K., Munot, A., and Kumar, K. R. (2002). On forecasting the indian summer monsoon: the intriguing season of 2002. *CURRENT SCIENCE-BANGALORE-*, 83(4):394–403.

Gilli, E. (1999). Evidence of palaeoseismicity in a flowstone of the observatoire cave (monaco). *Geodinamica Acta*, 12(3):159–168.

Gilli, E. (2005). Review on the use of natural cave speleothems as paleoseismic or neotectonics inidicators. *Comptes Rendus Geoscience*, 337:1208–1215.

Gogoi, B., Deka Kalita, K., Garg, R., and Borgohain, R. (2009). Foraminiferal biostratigraphy and palaeoenvironment of the lakadong limestone of the mawsynram area, south shillong plateau, meghalaya. *Journal of the Palaeontological Society of India*, 54(2):209.

Grinsted, A., Moore, J. C., and Jevrejeva, S. (2004). Application of the cross wavelet transform and wavelet coherence to geophysical time series. *Nonlinear processes in geophysics*, 11(5/6):561–566.

Guilyardi, E. (2006). El niño–mean state–seasonal cycle interactions in a multi-model ensemble. *Climate Dynamics*, 26(4):329–348.

Holden, N. E. (1989). Total and spontaneous fission half-lives for uranium, plutonium, americium and curium nuclides. *Pure and Applied Chemistry*, 61(8):1483–1504.

Jaffey, A., Flynn, K., Glendenin, L., Bentley, W. t., and Essling, A. (1971). Precision measurement of half-lives and specific activities of u 235 and u 238. *Physical Review C*, 4(5):1889.

Kagan, E. J., Agnon, A., Bar-Matthews, M., and Ayalon, A. (2005). Dating large infrequent earthquakes by damaged cave deposits. *Geology*, 33(4):261–264.

Kawamura, R., Uemura, K., and Suppiah, R. (2005). On the recent change of the indian summer monsoon-enso relationship. *SOLA*, 1:201–204.

Khattri, K. (1992). *Seismological investigations in north eastern region of India*. Department of Earth Sciences, University of Roorkee.

Krishnamurthy, V. and Goswami, B. N. (2000). Indian monsoon-enso relationship on interdecadal timescale. *Journal of Climate*, 13(3):579–595.

Kumar, K. K., Rajagopalan, B., and Cane, M. A. (1999). On the weakening relationship between the indian monsoon and enso. *Science*, 284(5423):2156–2159.

Kumar, K. K., Rajagopalan, B., Hoerling, M., Bates, G., and Cane, M. (2006). Unraveling the mystery of indian monsoon failure during el nino. *Science*, 314(5796):115–119.

Lachniet, M. S. (2009). Climatic and environmental controls on speleothem oxygen-isotope values. *Quaternary Science Reviews*, 28(5):412–432.

Lee, T. and McPhaden, M. J. (2010). Increasing intensity of el niño in the central-equatorial pacific. *Geophysical Research Letters*, 37(14).

Lenton, T. M., Held, H., Kriegler, E., Hall, J. W., Lucht, W., Rahmstorf, S., and Schellnhuber, H. J. (2008). Tipping elements in the earth's climate system. *Proceedings of the National Academy of Sciences*, 105(6):1786–1793.

Ludwig, K. (2010). Using isoplot/ex, version 3.75: A geochronological toolkit for microsoft excel. *Berkeley Geochronology Center Special Publication*, 1a:47.

Ludwig, K., Wallace, A. R., and Simmons, K. (1985). The schwartzwalder uranium deposit; ii, age of uranium mineralization and lead isotope constraints on genesis. *Economic Geology*, 80(7):1858–1871.

Martín-García, R., Alonso-Zarza, A. M., and Martín-Pérez, A. (2009). Loss of primary texture and geochemical signatures in speleothems due to diagenesis: Evidences from castañar cave, spain. *Sedimentary geology*, 221(1):141–149.

MeghalayaPopulation (2013). Population census 2011, meghalaya population census data 2011. http://www.census2011.co.in/census/state/meghalaya/. Accessed: 2013-03-01.

Miller, A. J., Cayan, D. R., Barnett, T. P., Graham, N. E., and Oberhuber, J. M. (1994). The 1976–77 climate shift of the pacific ocean. *Oceanography*, 7(1):21–26.

Morino, M., Maksud Kamal, A., Muslim, D., Ekram Ali, R. M., Kamal, M. A., Zillur Rahman, M., and Kaneko, F. (2011). Seismic event of the dauki fault in 16th century confirmed by trench investigation at gabrakhari village, haluaghat, mymensingh, bangladesh. *Journal of Asian Earth Sciences*, 42(3):492–498.

Niranjan Kumar, K., Rajeevan, M., Pai, D., Srivastava, A., and Preethi, B. (2013). On the observed variability of monsoon droughts over india. *Weather and Climate Extremes*, 1:42–50.

Panno, S. V., Lundstrom, C. C., Hackley, K. C., Curry, B. B., Fouke, B. W., and Zhang, Z. (2009). Major earthquakes recorded by speleothems in midwestern us caves. *Bulletin of the Seismological Society of America*, 99(4):2147–2154.

Parthasarathy, B., Munot, A., and Kothawale, D. (1995). *Monthly and seasonal rainfall series for All-India homogeneous regions and meteorological subdivisions, 1871-1994*. Indian Institute of Tropical Meteorology.

Reddy, D., Nagabhushanam, P., Kumar, D., Sukhija, B., Thomas, P., Pandey, A. K., Sahoo, R., Ravi Prasad, G., and Datta, K. (2009). The great 1950 assam earthquake revisited: Field evidences of liquefaction and search for paleoseismic events. *Tectonophysics*, 474(3):463–472.

Richards, D. A. and Dorale, J. A. (2003). Uranium-series chronology and environmental applications of speleothems. *Reviews in Mineralogy and Geochemistry*, 52(1):407–460.

Saikia, M. M. (1981). Seismicity of the north-eastern region (ner) of india. *Studia Geophysica et Geodaetica*, 25(1):36–60.

Shukla, R. P., Tripathi, K. C., Pandey, A. C., and Das, I. (2011). Prediction of indian summer monsoon rainfall using niño indices: a neural network approach. *Atmospheric Research*, 102(1):99–109.

Sinha, A., Berkelhammer, M., Stott, L., Mudelsee, M., Cheng, H., and Biswas, J. (2011). The leading mode of indian summer monsoon precipitation variability during the last millennium. *Geophysical Research Letters*, 38(15).

Sukhija, B., Rao, M., Reddy, D., Nagabhushanam, P., Hussain, S., Chadha, R., and Gupta, H. (1999). Timing and return period of major palaeoseismic events in the shillong plateau, india. *Tectonophysics*, 308(1):53–65.

Trenberth, K. E. (1990). Recent observed interdecadal climate changes in the northern hemisphere. *Bulletin of the American Meteorological Society*, 71(7):988–993.

Trenberth, K. E. and Stepaniak, D. P. (2001). Indices of el niño evolution. *Journal of Climate*, 14(8):1697–1701.

USGS (2014). USGS Earthquake Hazards Program historic earthquakes, assam-tibet, 1950 august 15. http://earthquake.usgs.gov/earthquakes/world/events/1950_08_15.php. Accessed: 2014-07-09.

Wang, Y., Cheng, H., Edwards, R. L., Kong, X., Shao, X., Chen, S., Wu, J., Jiang, X., Wang, X., and An, Z. (2008). Millennial-and orbital-scale changes in the east asian monsoon over the past 224,000 years. *Nature*, 451(7182):1090–1093.

Yeh, S.-W., Kug, J.-S., Dewitte, B., Kwon, M.-H., Kirtman, B. P., and Jin, F.-F. (2009). El niño in a changing climate. *Nature*, 461(7263):511–514.

Yu, J.-Y., Zou, Y., Kim, S. T., and Lee, T. (2012). The changing impact of el niño on us winter temperatures. *Geophysical Research Letters*, 39(15).

Zhou, T.-J. and Yu, R.-C. (2005). Atmospheric water vapor transport associated with typical anomalous summer rainfall patterns in china. *Journal of Geophysical Research: Atmospheres (1984–2012)*, 110(D8).